# Analysis of a Segmented Axial Active Magnetic Bearing for Multi-MW Compressor Applications

Rafal Piotr Jastrzebski, *Senior Member, IEEE*, and Olli Liukkonen

***Abstract*—In high-speed compressor and turbine applications, active magnetic bearings are employed to increase reliability, reduce maintenance, and provide contact-free and oil-free operation. Evidently, the dynamic performance of active magnetic bearings must correspond to application-specific events like compressor surge or thrust disturbances. This article presents a segmented stator as one of the solutions to increase the bandwidth of axial active magnetic bearings (AMBs) and further improve the stability of the shaft system. We analyze the effects and discuss the tradeoffs of axial active magnetic bearing stator segmentation and slitting to alleviate bandwidth limitations. Finite element method design optimization and control plant modeling methods, open- and closed-loop tests, and identification of the overall thrust AMB–rotor control plant are studied.**

***Index Terms*—Axial active magnetic bearing, digital control, eddy currents, finite element method (FEM), magnetic levitation, vibration analyses.**

## I. Introduction

THE motion control of magnetically levitated rotors in compressor and turbine applications can bring substantial application benefits despite being somewhat challenging to implement. Temperature differences can affect wheel clearances and operating conditions, which are key in establishing an optimal flow and performance. Process flow changes, external thrust synchronous forces, variable loads, and displacement sensor runout can cause closed-loop control oscillations and flow oscillations leading to instabilities including surge [1], [2], [3].

The closed-loop performance of active magnetic bearings (AMBs) is limited by the capacity, linearity, and bandwidth of the electromagnetic actuators, limitations of feedback sensors and drivers, delays, and the control algorithm itself [4]. Specifically in axial AMBs, the bandwidth is limited by the magnetic circuit of the actuator. The stator core of the actuator is made of solid steel to ensure a mechanically rigid structure. The drawback of this solution is the eddy currents, which have an impact on performance [5]. The required bandwidth of an axial AMB is an important parameter already in the design phase of the compressor–motor system, and therefore, the effect of eddy currents should be predicted and further minimized [6]. Solutions to this issue consider stator core segmentation. The properties of solid and segmented core AMBs have been modeled, for instance, in [7] and [8]. Spece et al. [9] proposed optimization of the geometry based on models from [7]. These studies focused on linearized forces, small-signal amplitudes, and using the finite element method (FEM) as a reference. However, it is not clear how to best simulate and measure the influence of AMB geometry and eddy currents on the actuator bandwidth. So far, the details of segmentation or slitting design, manufacturing, and practicality in different applications have not been addressed sufficiently in the literature. Moreover, the majority of applications relate to relatively small powers [10]. In [11], the general design of a stand-alone multimegawatt (MMW) rotor, an optimized radial actuator geometry with flux barriers for zero bias operation, and radial levitation control were presented. The initial version of the slit axial actuator design and some results of static force simulations were shown.

In this article, we use the same MMW rotor, but analyze the performance of the optimized axial AMB with a slit stator for a compressor application. We address the following questions: How do eddy currents affect the force slue rate and bandwidth of the axial AMB actuator? How can slitting or stator segmentation improve performance? What are the risks and what is compromised when slits or segmentation are applied? How can geometry features (slit depth and number) be optimized? Finally, how can the overall control plant employing a slit AMB stator be modeled and identified for control purposes in MMW compressor applications?

The major novelties of this study can be listed as follows.

1) Quantitative bandwidth estimation of solid and slit versions of a thrust magnetic force actuator by using various modeling and measurement methods.
2) Electromechanical modeling and parametric identification of the control system based on experimental frequency responses of the drivetrain.

The research questions are considered from the viewpoints of modeling and testing, leading to several findings that can be employed in further research work:

Manuscript received 27 June 2022; revised 11 October 2022, 13 December 2022, 30 December 2022, and 1 March 2023; accepted 3 March 2023. Recommended by Technical Editor Z. Zhu and Senior Editor Y. Li. *(Corresponding author: Rafal Piotr Jastrzebski.)*

Rafal Piotr Jastrzebski is with the Department of Electrical Engineering, Lappeenranta-Lahti University of Technology, 53850 Lappeenranta, Finland, and also with the Department of Mechanical and Materials Engineering, University of Turku, 20014 Turku, Finland (e-mail: rafal.jastrzebski@lut.fi).

Olli Liukkonen is with the Department of Electrical Engineering, Lappeenranta-Lahti University of Technology, 53850 Lappeenranta, Finland, and also with the ABB Oy, 00380 Helsinki, Finland (e-mail: Olli.Liukkonen@lut.fi).

Color versions of one or more figures in this article are available at https://doi.org/10.1109/TMECH.2023.3254812.

Digital Object Identifier 10.1109/TMECH.2023.3254812

1) The time-stepping 3-D FEM method with sinusoidal excitation provides the most numerically stable and accurate bandwidth estimate for design optimization and modeling purposes.
2) A comparison of different experimental validation methods shows that the measured force step responses give a rough qualitative estimate and comply with the simulated step responses. However, measured sinusoidal excitation responses, like FEM simulations, provide the most reliable quantitative bandwidth estimate.
3) The effect of excitation type and amplitude significantly influence the estimated bandwidth values.

The rest of this article is organized as follows. In Section II, we introduce the preliminaries of the force actuation, analytical formulas, and the underlying modeling challenges. In Section III, the 2-D and 3-D FEM methods used for design considerations are shown. Improving the design performance by construction allows a higher bandwidth control, while practical evaluation in the application enables feasibility assessment from a wider perspective. The performance of the manufactured variant of the AMB can be tested according to the measurement methods introduced in this section. Next, we propose a parametric control plant model, which is suitable for the model-based control in the operating point. Section IV details the simulation and measurement results, bandwidth estimates, and closed-loop identification of the installed axial AMB in the multirotor drivetrain. The plant model parameters are tuned to the measured responses. Then, in Section V, we discuss differences between simulations and experiments, experimental and modeling challenges, and the significance of higher order dynamics, and compare the manufacturing costs. Finally, the conclusions presented in Section VI answer the research questions formulated in the introduction, and the Appendix gathers the relevant parameters of the manufactured bearing.

## II. Preliminaries

A conventional thrust AMB contains electromagnets acting in opposition to generate bidirectional force along the geometrical symmetry axis. Each electromagnet acts as a stator of the axial actuator with a coil placed between two concentric poles. The attractive force exerted on the moving disc attached to the rotor is generated toward the pole surfaces. The analytical expression for magnetic force is computed applying the principles of virtual work. The partial derivative of the magnetic co-energy $W_{\mathrm{ce}}$ with respect to the virtual displacement $z$ equals

$$F_z = \frac{\partial W_{\mathrm{ce}}}{\partial z} = \frac{B^2 S}{\mu_0} \tag{1}$$

where $\mu_0$ is the permeability of air, and $S$ is the pole area. Fig. 1 shows the manufactured slit AMB stator with the outer and inner pole areas indicated in the figure, each equal to $S$. Fig. 2 provides a sectional view of the geometry with the main dimensions, given in the Appendix. From the magnetic circuit approximation of the main flux path, with the help of Ampere's circuital law, assuming infinite permeability of iron and no fringing and leakage fluxes,

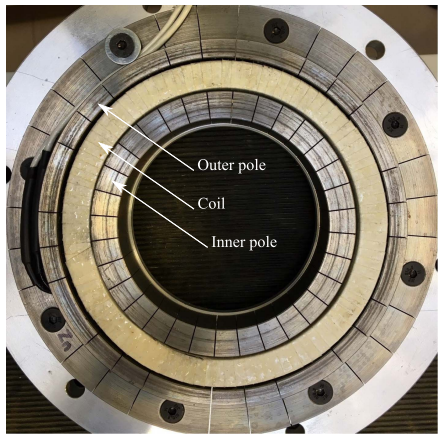


Fig. 1. Stator core made from S355J2 with 32 slits. The construction parameters are given in Table III and in Appendix.

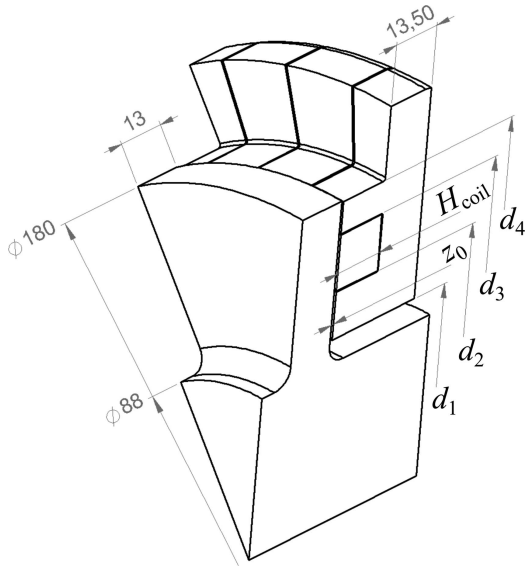


Fig. 2. Main dimensions of the AMB stator and rotor according to Table III from Appendix. The stator yoke is elongated for mechanical mounting reasons.

the magnetic flux density $B$ at the nominal air gap $z_0$ becomes

$$B = \mu_0 \frac{Ni}{2z_0}. \tag{2}$$

$N$ is the number of turns in the coil and $i$, is the coil current.

Using the air-gap reluctance $\Re = z_0/(\mu_0 S)$ and substituting (2) to (1), the force and the inductance can be expressed as follows:

$$F_z = \frac{L^2 i^2}{\mu_0 N^2 S}, L = \frac{N^2}{2\Re}. \tag{3}$$

The initial analytical force production bandwidth can be estimated using the force amplitude approximation as a function of the frequency $f$ dependent inductance $L(f)$ and the current

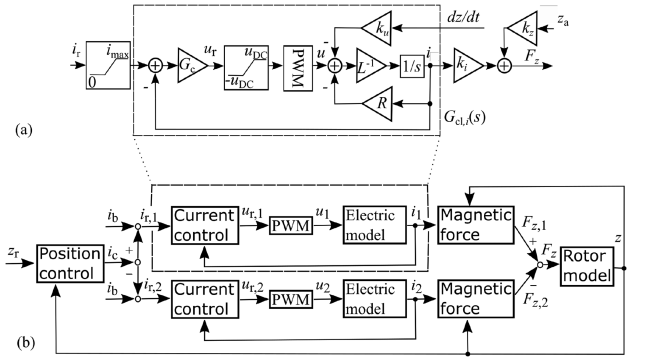


Fig. 3. (a) Inner current control loop and the force-producing mechanism for a single electromagnet. In the simple linear model, the PWM delay, voltage and current saturation, and the velocity-induced voltage coefficient $k_u$ are neglected, resulting in (5). (b) Simplified cascade control structure of an axial AMB. The signal saturation and dependence of the electric model on rotor position are neglected.

amplitude $i(f)$

$$F_z(f) = \frac{L^2(f) i^2(f)}{\mu_0 N^2 S}. \tag{4}$$

However, the current amplitude will depend on the inner current control dynamics of the AMB amplifier, which will also change with the frequency.

Typically, the AMB control structure comprises outer position and inner current controllers. The inner current control loop dynamics (Fig. 3) can be approximated as a transfer function

$$G_{\mathrm{cl},i}(s) = \frac{G_\mathrm{c}}{sL + R + G_\mathrm{c}}. \tag{5}$$

It acts as a filter applied to the reference current $i_\mathrm{r}$. $s$ is the Laplace variable, and $G_\mathrm{c}(s)$ is the transfer function of a current controller (e.g., PID). Based on this filtered (measured) current $i_\mathrm{m} = G_{\mathrm{cl},i} i_\mathrm{r}$, the force response can be interpolated from the analytical force equation (4). With digital control implementation, the performance will be affected by the zero order hold, control transportation delays, and pulse width modulation (PWM).

Equation (5) looks like a linear system, but in fact, the parameters are frequency (and signal amplitude) dependent. The resistance $R$ is a sum of the copper resistance $R_\mathrm{cu}$, which will increase as a function of frequency because of the skin effect and the resistance $R_\mathrm{e}$ according to eddy currents on the surfaces of the nonlaminated iron of the actuator (mostly in the stator and rotor pole areas). Combining these into the complex actuator coil impedance yields

$$Z(\omega) = R_\mathrm{cu}(\omega) + R_\mathrm{e}(\omega) + j\omega L(\omega) \tag{6}$$

with $\omega = 2\pi f$. In a basic case, the internal current controller can be designed as a proportional gain selected as a ratio of the dc link voltage $u_\mathrm{DC}$ and the maximum current $G_\mathrm{c} = u_\mathrm{DC}/i_\mathrm{max}$. For the basic controller, $s = j\omega$, and $R = R_\mathrm{cu} + R_\mathrm{e}$, (5) becomes

$$G_{\mathrm{cl},i}(s) = \frac{u_\mathrm{DC}}{(R + sL) i_\mathrm{max} + u_\mathrm{DC}}. \tag{7}$$

For a single electromagnet, the magnetic force (3), which is dependent on the coil current $i$ and the air gap $z_\mathrm{a}$, is modeled with the current stiffness $k_i$ and the negative position stiffness $k_z$ in Fig. 3(a).

In most applications there is a need for a magnetic force over a single (or each) control axis in two opposite directions. This is typically achieved with pairing of two electromagnets opposite to each other. The force is linearized by a cascade control structure and a differential driving mode. In the inner loops we superimpose the bias current $i_\mathrm{b}$ to the outer loop control current $i_\mathrm{c}$ so that the reference currents of the inner loops are $i_\mathrm{r} = i_\mathrm{b} \pm i_\mathrm{c}$. In turn, using (3), the force produced by the pair of opposite electromagnets, controlled by the outer-loop position controller, near the central (rotor) position yielding the air gaps $z_\mathrm{a} = z_0 \mp z$, is a function of the rotor displacement $z$ and the control current $i_\mathrm{c}$

$$F_z = \frac{\mu_0 N^2 S}{4} \left( \frac{(i_\mathrm{b} + i_\mathrm{c})^2}{(z_0 - z)^2} - \frac{(i_\mathrm{b} - i_\mathrm{c})^2}{(z_0 + z)^2} \right). \tag{8}$$

The cascaded control structure of the axial AMB is shown in Fig. 3(b), where the axial position controller $G_\mathrm{c}$ can be computed as for the radial one, e.g., as presented in [11]. Using this differential driving mode and control cascade with the mechanical clearance $z_\mathrm{max} \leq z_0/2$ and for the maximum control current $i_\mathrm{cmax} = i_\mathrm{b}$, the static (not dependent on frequency) force relation does not significantly deviate from the linear one (being typically 5% nonlinear, but depending on the steel used, can be more, e.g., for currents, leading to magnetic saturation)

$$F_z = k_i i_\mathrm{c} + k_z z. \tag{9}$$

For a linear outer position controller synthesis, the current stiffness $k_i$ and the position stiffness $k_z$ in the linearized force are defined in the operating point ($z = 0$, $i_\mathrm{c} = 0$)

$$k_i = \frac{\mu_0 N^2 S i_\mathrm{b}}{z_0^2}, k_z = \frac{\mu_0 N^2 S i_\mathrm{b}^2}{z_0^3}. \tag{10}$$

The values of force coefficients for two opposing electromagnets in (10) are doubled compared with the ones for the single electromagnet from Fig. 3(a).

## III. Methods

We are looking for methods to quantify the performance of different design variants and analyze the impact of eddy currents on the actuator force parameters and dynamics. The dimensions of the axial AMB of the 2 MW electrical machine prototype, measured and analyzed by the FEM, are according to [11] and [12] (see Figs. 1, 2, and Appendix). The FEM simulations are made in JMAG Designer 18.1. Opposite electromagnets and the shaft are modeled to accommodate fringing and leakage effects. The sections of the studied geometries according to different numbers of slits (see Fig. 4) and for different slit depths (see Fig. 5) are investigated. The selected manufactured geometry is later measured on the lab table, in the identification rig using a force transducer cell according to Fig. 6, and finally in the application as in Fig. 7.

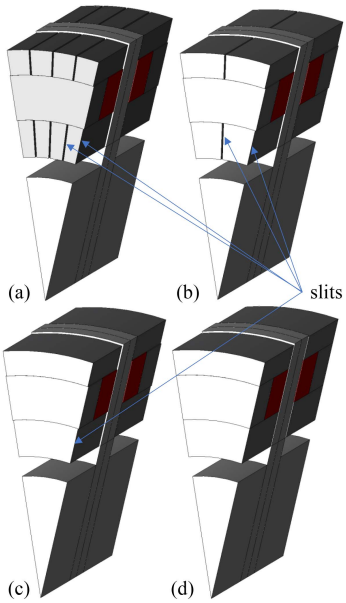


Fig. 4. Sections of the studied geometries according to different numbers of slits: (a) 64, (b) 32, (c) 16 (slits coincide with the section cuts), (d) solid. The coil, stator, and rotor iron are depicted in red, dark gray, and light gray, respectively.

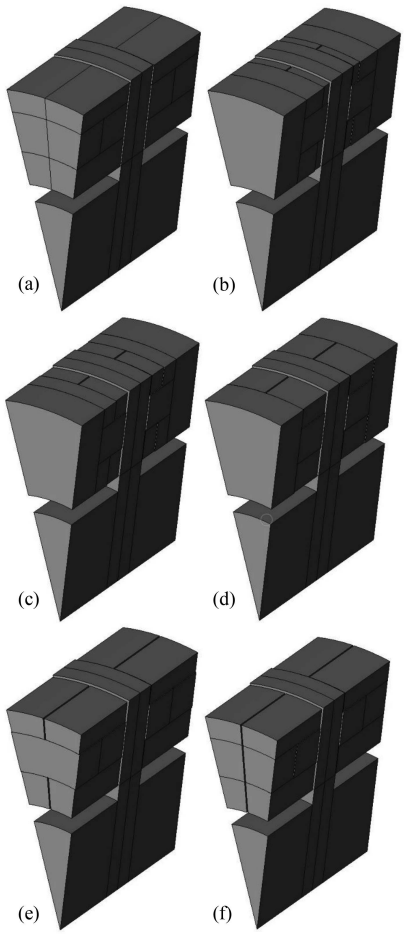


Fig. 5. Studied geometries for a solid stator and stator with 32 slits according to variable slit depth. (a) Solid (line is for modeling purposes), (b) 3.5 mm, (c) 7 mm, (d) 14 mm, (e) 28 mm, (f) segmented.

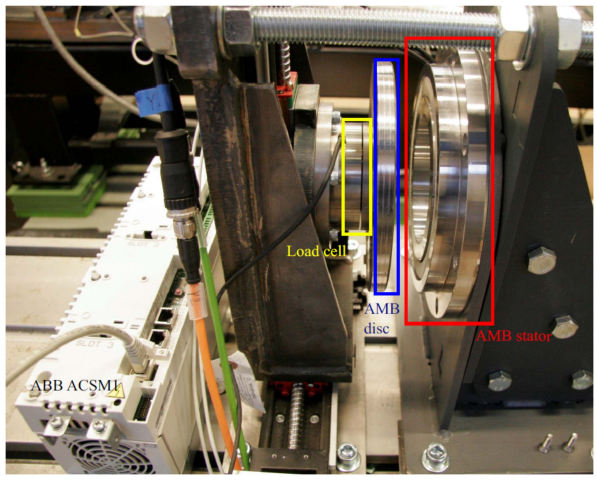


Fig. 6. Measurement of the step force responses of the axial AMB using the force load cell (Mini85 from ATI Industrial Automation) and an ABB's ACSM1-04AM-016A-4 inverter. Two different stator structures are compared in the measurements. In the photo, the air gap is widened to show the solid stator structure.

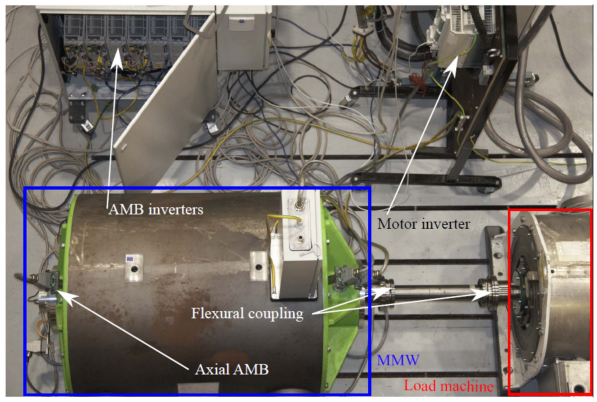


Fig. 7. Measurement setup for the frequency characteristics of an axial AMB in the 2 MW AMB–rotor [11] connected with a flexural coupling to the load.

### A. 3-D FEM Static Simulations

For computation of force capacity, static simulations are carried out in the 3-D FEM at the zero speed with 0.5 mm and smaller mesh element sizes on active pole surfaces. The number of elements varies from 649811 for the solid stator and up to 1050108 for the segmented (slit) stators. The bandwidth of the inductor $f_{\mathrm{BW,l}}$ with a zero resistance (from the input voltage to the coil current) can be drawn, for instance, based on the large-signal inductance $L_{\mathrm{l}} = \Psi_{\max}/i_{\max}$ and the step response (calculated from 0.1 to 0.9 of the steady state value) using the dc link voltage

$$f_{\mathrm{BW,l}} = \frac{\ln(9)}{2\pi} \frac{u_{\mathrm{DC}}}{L_{\mathrm{l}} i_{\max}}. \tag{11}$$

The saturation makes the estimated inductance dependent on current amplitude, especially when computed using the coil flux linkages $\Psi_{\max}$ that appear with maximum current amplitudes. For improved accuracy, small-signal inductance values can be

computed from the coil flux linkages $\Psi$ for the currents $i$, e.g., at every 2 A up to the maximum amplifier current $i_{\max}$ and at the nominal air gap $L_{\rm s}(i) = \Delta\Psi/\Delta i$. Then, the value of the current bandwidth will depend on the rise time $t_{\rm r}$

$$f_{{\rm BW},t_{\rm r}} = \frac{\ln(9)}{2\pi t_{\rm r}}, \tag{12}$$

$$t_{\rm r} = \frac{1}{u_{\rm DC}} \int_0^{i_{\max}} L_{\rm s}(i)di. \tag{13}$$

Furthermore, the effects of magnetic saturation on force production can be taken into account in the force bandwidth based on the Bode magnitude drop from (7) or on the rise time from (12) when applying a 3-D FEM static force map computed as a function of current. However, because the eddy currents are not taken into account, those bandwidth estimates are still overoptimistic as shown in the results section below.

### B. 3-D FEM Time-Stepping Simulations

To overcome the limitations of static simulations, the dynamic force response bandwidth is estimated using 3-D FEM time-stepping. Two methods are used.

First, the bandwidth can be approximated directly based on the rise time $t_{\rm r}$ (of force) from 0.1 to 0.9 times the steady-state force in response to the step current and using (12). The force rise rate $dF/dt$ is high at the beginning of the simulation, and therefore, a variable step size sequence is used where the step sizes follow increasing powers of 2 (from $2^1$ to $2^{10}$) in consecutive sequences. The numbers of elements are from 170598 to 181692 for 22.5° sections of AMBs with a symmetry condition to allow reasonable simulation times on a desktop PC.

Second, the alternative dynamic force response is studied from a series of simulations when applying sinusoidal currents of different frequencies and amplitudes. For each frequency, the simulation time and step size should be adjusted in order to dissipate transients and maintain accuracy (a constant number of steps in the excitation period). Frequency response force magnitude (to each current amplitude) equivalent Bode plots can be constructed for the simulated frequency points, and the force bandwidth can be interpolated from the plot at a –3 dB (0.708 absolute) amplitude drop. We found this last simulation method to be faster and more numerically stable than the force step responses, which are dependent on the particular FEM solver settings and time step division sequences.

### C. LR Serial Model Measurements With a Bench LCR Meter

Owing to the FEM analysis, the 32-slit stator version was selected for manufacturing as a compromise between manufacturing cost, mechanical integration, and bandwidth improvement over the solid stator. Electrical discharge machining was used to cut radial grooves with a 0.5-mm width and a 28-mm depth in the slit stator core (Fig. 1).

The most straightforward bandwidth measurement can be performed by using an *LCR* meter. *LR* serial model parameters of the AMB with the solid stator and the stator with 32 slits are compared.

The serial model measurements of the electromagnetic actuator were made using a Model 891 300 kHz Bench LCR Meter by B&K Precision Corporation. The accuracy varies (depending on the measured value and according to the manufacturer's accuracy charts) in the range of 0.5–1% for $R$ and $L$ at 1 Vrms. Measurements are made with a 0.5 mm thick plastic sheet enforcing the constant air gap under compression on the lab table.

The current bandwidth (–3 dB) can be computed for measured serial model parameters according to (7). However, the mapping between the current and the force is not linear, and the serial model parameter values depend on the current amplitudes in addition to the air gap. The *LCR* meter applies very small and not constant current amplitudes when changing frequency.

### D. LR Serial Model Measurements With an AC Supply

The measurements at a higher constant current amplitude of 2 A were made with a programmable Pacific Power 360AMX ac supply. The voltages and currents were captured with a Rhode&Schwarz RTO 1014 oscilloscope and processed to estimate the series equivalent $R(f)$ and $L(f)$ at each frequency point.

In order to estimate the force generation performance for yet higher amplitudes, the numerical results could be extrapolated by using FEM static electromagnetic solutions or analytical force equations, e.g., (3). If the measurements are made at known higher current amplitudes (but at a variable voltage), the bandwidth can be calculated directly from the force equations.

However, the AMB coils are driven by inverters using current regulation that is constrained by the feedback, control delays, dc link voltage limit, and eddy current effects. Further, the current to force mapping is constrained by the static magnetic nonlinearity. Therefore, the bandwidth of the force response is significantly reduced compared with the inductor current response bandwidth.

The current amplitude $i$ can be adjusted to take into account the closed-loop inner current control dynamics $G_{\rm cl}$ (filtering) because of the additional amplitude drop as a function of frequency when linearized for every frequency point $f$.

### E. Step Force Measurement

The step responses from the 3-D FEM can be verified experimentally using the force transducer mounted on the rotor shaft [13], [14]. The rigid mounting of the AMB disc and the stator should prevent relative movements, vibrations, and changes in the air gap (Fig. 6). The resolution of the force transducer type Mini85 from ATI Industrial Automation used in the study is 0.32 N, and the measurement bandwidth is 5 kHz. In the step force and the following frequency response measurements, the stator coils are driven using ABB ACSM1-04AM-016A-4 inverters [11]. This means that the results include the effects of the inner-loop current control dynamics unlike in the case of the FEM.

### F. Frequency Responses and Identification of the Axial AMB–Rotor Plant Model

In this study, the AMBs were controlled using standard industrial drive and automation components [15] [11]. From the viewpoint of the outer position controller, the overall dynamics of the AMB–rotor, when using a differential driving mode and a cascade control configuration, are affected by the electromagnetic actuator, the inner current controller, and the axial rotor dynamics. In this study, the model-based $H$-infinity controller is used in the identification measurements. The control scheme is identical to the radial AMB controller presented in [11]. Axial AMBs can be used for rotors with integrated compressors (or turbines) or for multirotor systems connected by various means (e.g., couplings, thin shafts, etc.). In some applications, axial vibrations can occur at various frequencies. At lower frequencies, they can affect the position control performance and stability.

The basic mechanical model of the axial AMB–rotor is a point mass represented by a double integrator. Using a more accurate plant model for the position controller synthesis will improve the closed-loop control performance. In the application, the plant frequency responses can be identified using AMB forces and sensor signals. Based on these frequency responses, the linearized parametric plant model $G_z(s)$ can be derived. Relating to the physical plant and taking the MMW drivetrain as an example [12], the model can be assembled, comprising the rigid rotor mode $G_0(s)$, two torsional modes (or lateral or stator mounting/tubing modes) $G_1(s)$ and $G_2(s)$ in a parallel connection, and the actuator frequency response matching dynamics $G_\mathrm{a}(s)$ in a series connection.

$$G_z(s) = G_\mathrm{a}(s)(G_0(s) + G_1(s) + G_2(s)), \tag{14}$$

$$G_\mathrm{a}(s) = \frac{s/\omega_{2\mathrm{z}} + 1}{s/\omega_{2\mathrm{p}} + 1} \cdot \frac{s/\omega_{1\mathrm{z}} + 1}{s/\omega_{1\mathrm{p}} + 1} \cdot \frac{1}{s/\omega_{0\mathrm{p}} + 1} \tag{15}$$

where $\omega$ represents the corner frequency of the corresponding poles and zeros. The mechanical series model

$$G_0(s) + G_1(s) + G_2(s) = \frac{k_i}{m_0 s^2 - k_z} + \frac{d_1 k_i}{s^2 + 2\zeta_1\omega_1 s + \omega_1^2} + \frac{d_2 k_i}{s^2 + 2\zeta_2\omega_2 s + \omega_2^2}. \tag{16}$$

$m_0$ is a rotor mass of the model. The resonant modes represented by the complex pole pairs are constructed using corner frequencies, e.g., $\omega_1 = 2\pi f_1$ ($f_1$ being equal to the frequency response peaks), the relative damping $\zeta_1$, and the mode shape scaling coefficient $d_1$.

The proposed parametric model can be used for various position control strategies including optimal model-based control methods.

## IV. Results

### A. Electromagnetic Simulation and Analytical Results

Geometries with different numbers of slits (Fig. 4) and with a variable slit depth (Fig. 5) are studied. First, static simulations are performed. Fig. 8 presents a flux contour plot for the maximum peak amplifier current of a section of the AMB with 32 slits. Fig. 9 shows the increasing forces $f_z$ with current. For a more segmented stator, the force decreases slightly because of the stator cuts influencing the effective pole area. The small-signal inductance also decreases with an increasing current and with the number of segments.

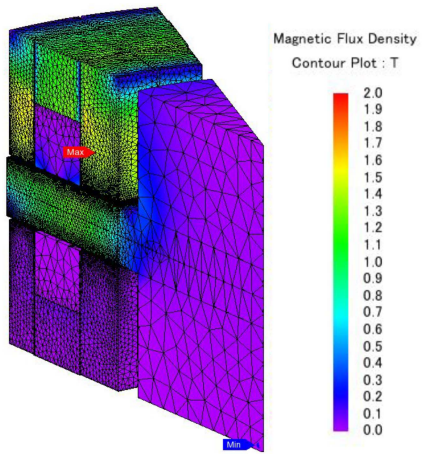


Fig. 8. Magnetic flux contour plot and mesh of a 22.5° 3-D section of the axial AMB with 32 slits at the maximum amplifier peak current.

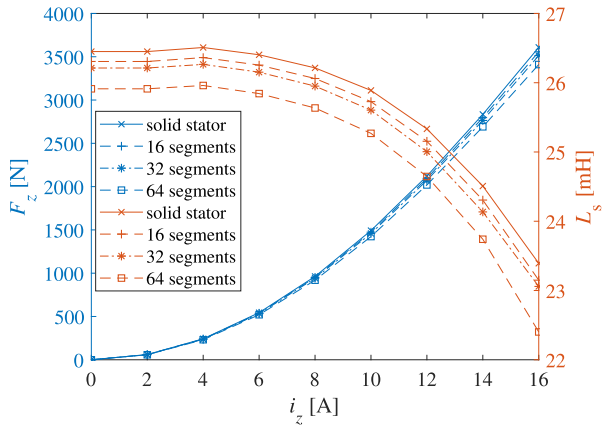


Fig. 9. Static forces and small-signal inductances from 3-D FEM.

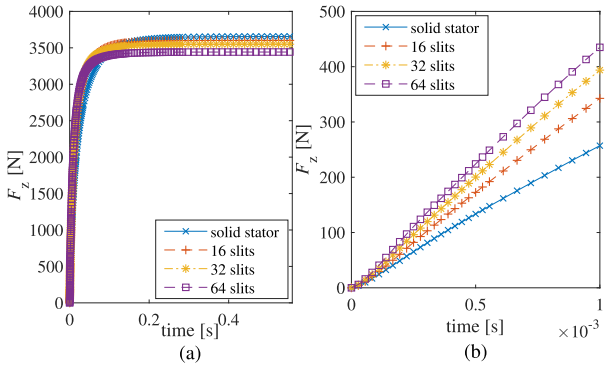


Fig. 10. Force changes in the time-stepping 3-D FEM simulation. Bandwidth estimates are given in Table I, $f_{\mathrm{BW},t_\mathrm{rise}}$.

TABLE I
BANDWIDTH ESTIMATES BASED ON SIMULATED STATIC AND DYNAMIC RESPONSES FOR MAXIMUM CURRENT AMPLITUDES. (ANALYTICAL SMALL-SIGNAL ESTIMATE FOR A SEGMENTED STATOR [8].)

| Stator | $L_\mathrm{l}$ | $f_{\mathrm{BW,l}}$ | $f_{\mathrm{BW},t_\mathrm{rise}}$ | $f_{\mathrm{BW},-3\mathrm{dB}}$ ([8]) |
|---|---|---|---|---|
| Solid | 25.6 mH | 373 Hz | 4.8 Hz | 8.9 Hz (80 Hz) |
| 16 slits | 25.4 mH | 376 Hz | 7.8 Hz | 13.4 Hz (179 Hz) |
| 32 slits | 25.3 mH | 378 Hz | 8.9 Hz | 15.6 Hz (241 Hz) |
| 64 slits | 24.9 mH | 384 Hz | 10.8 Hz | 18 Hz (306 Hz) |

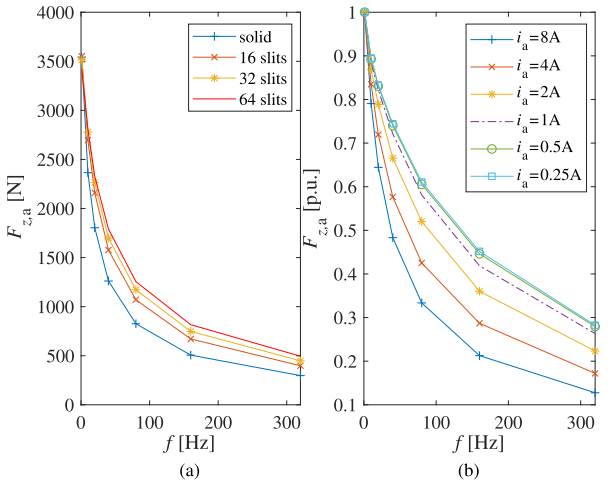


Fig. 11. Force amplitudes as a function of frequency from the 3-D FEM section study. (a) Force for different numbers of slits (Table I, $f_{\mathrm{BW},-3\mathrm{dB}}$). (b) Normalized force at different sinusoidal current amplitudes $i_\mathrm{a}$ for the 32 slit design with the 28-mm slit depth.

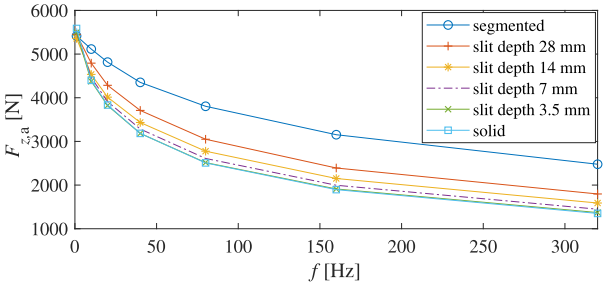


Fig. 12. Force dependence on the slit depth as a function of frequency.

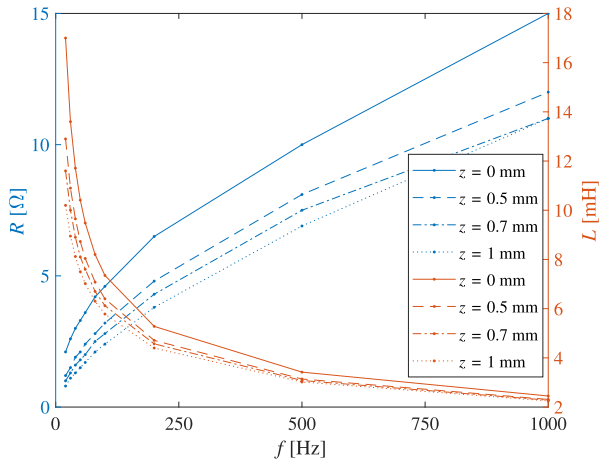


Fig. 13. Serial model measurements of AMB with the 32-slit stator using the 891, 300-kHz bench *LCR* meter at different air gaps.

In Fig. 10, step force responses are shown for the rotors at 12000 r/min. Table I summarizes the bandwidth estimates based on the static and dynamic responses $f_{\mathrm{BW,l}}$ and $f_{\mathrm{BW},t_\mathrm{rise}}$. As a reference, analytical estimates of the small-signal bandwidth $f_{\mathrm{BW},-3\mathrm{dB}}$ [8] at the bias $i_\mathrm{b} = 0.5 \cdot i_\mathrm{max}$ are given. The simplified model for the segmented geometry with $n$ segments is

$$F_z(s) = \frac{\phi_\mathrm{b}}{\mu_0}\left(\frac{1}{A_1}+\frac{1}{A_2}\right)\left[\frac{N}{\frac{R_\mathrm{st}(s)+2R_\mathrm{g}(s)}{n}+R_\mathrm{r}(s)}\right]. \quad (17)$$

$\phi_\mathrm{b}$ is the bias flux, and $A_1$ and $A_2$ are the stator inner and outer pole face areas. $R_\mathrm{st}$, $R_\mathrm{g}$, and $R_\mathrm{r}$ are the stator, air-gap, and rotor reluctances of the form $R_i(s) = c_i\sqrt{s} + R_i^0$ resulting in a fractional order force function. $c_i$ and $R_i^0$ are the dynamic reluctance coefficient and the static reluctance computed based on the geometric parameters (given in the Appendix in Table III) of the iron cores [8].

Finally, Figs. 11 and 12 show results of the time-stepping simulation with sinusoidal currents. The bandwidth increases with an increasing number of slits, decreasing current amplitudes, and an increasing slit depth. The segmented stator yields the highest bandwidth.

## B. LR Serial Model Measurement Results

The inductance and resistance values obtained with the *LCR* meter and shown in Fig. 13 were measured for very small current amplitudes. As explained in the methods section, the current amplitudes are not constant when changing frequency. Therefore, we rely on *LR* serial model measurements with an ac supply instead of measurements made with an *LCR* meter for the force bandwidth estimate.

The measured inductance of the AMB with 32 slits in the stator is smaller than the static FEM-derived inductance as shown in Fig. 14(a) and in Table I. With a rise in the input frequency, the inductance drops while the resistance increases. Fig. 14(b) shows the estimated current $i_z$ and the force $F_z$ amplitudes from the closed-loop current feedback and the measured parameters. The force bandwidth estimate based on measurements at 2 A is 24 Hz for the AMB with 32 slits and 15 Hz for the AMB with the solid stator. The measurements were constrained by the minimum frequency, and therefore, to estimate the –3 dB force amplitude line, the inductance values at low frequencies had to be extrapolated.

For the small amplitudes, the force bandwidth increases. In fact, for two opposite AMB electromagnets operated in the differential driving mode with a bias (8), the bandwidth will increase by up to two times.

The measured $RL$ values based on a PACIFIC amplifier when compared with the 3-D FEM frequency responses [Fig. 15(a) based on Fig. 11(b)] show the same trend. However, the $RL$ estimates based on the FEM are smaller. For the AMB with the 32-slit stator, the force bandwidth estimate based on the FEM-derived $RL$ values at 1 A is 50 Hz and at 0.25 A is 60 Hz.

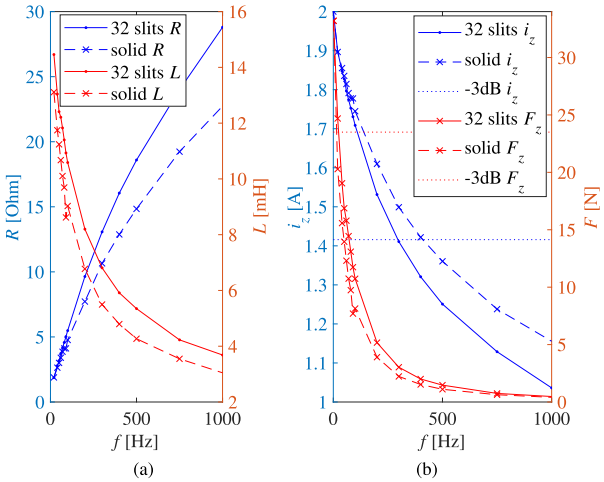


Fig. 14. (a) Serial model measurements at 0.7 mm and 2 A amplitude of sinusoidal current for one stator-rotor pair (electromagnet) and using a PACIFIC SmartSource 360-AMX ac Power Source and a Rhode&Schwarz RTO 1014 oscilloscope 1 GHz 10GSa/s. (b) Estimated frequency response based on the measured RL model, including inner current control dynamics, and static forces $F_z$ (3) computed based on resulting current amplitudes $i_z$ for each measured $RL$ value at each frequency. The corresponding force bandwidth estimates are given in Table II, $f_{\mathrm{BW},-3\mathrm{dB}}$.

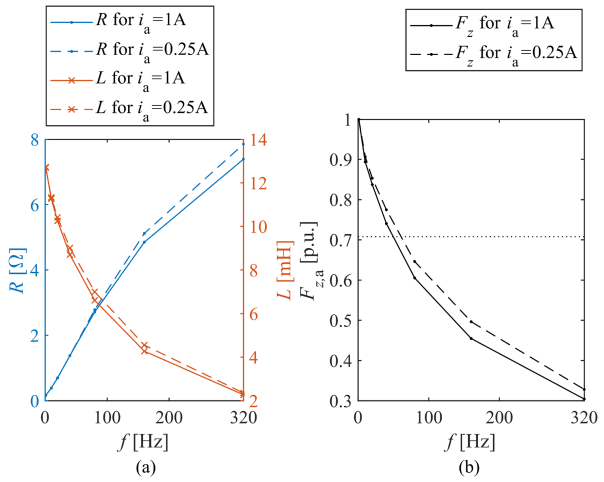


Fig. 15. (a) Serial model measurements of AMB with the 32 slit stator at 0.7 mm and for 0.25 A and 1 A amplitude of sinusoidal current $i_a$ for one stator reproduced in the 3-D FEM. (b) Force bandwidth estimate.

## C. Measured Step Force Responses

The identification (ID) rig [13] with the force cells fitted to the rotor has a limited force capacity when the axial AMB is placed in the rig. At maximum currents and at smaller air gaps, bending of the mechanical fitting occurred. Therefore, only force responses to the lower current amplitudes at a constant air gap of 0.7 mm are presented in Fig. 16. Fig. 17 shows faster rising reaction forces of the AMB with the slit stator compared with the solid stator for the same step currents. The responses show the same relations for different amplitudes with the 3-D FEM-computed step responses from Fig. 10. However, the rise times are even greater in measurements compared with the 3-D FEM simulations. Table II summarizes the bandwidth estimates

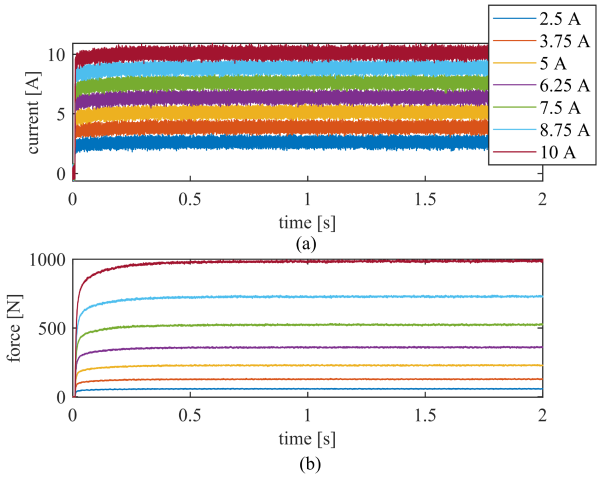


Fig. 16. Measured forces (b) for different step current amplitudes (a) applied to the AMB with the 32-slit stator.

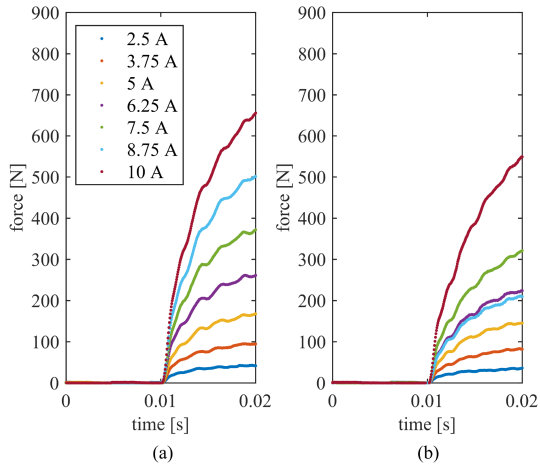


Fig. 17. Comparison of the measured forces with the different step current amplitudes applied to the AMB with the 32-slit stator (a) and with the solid stator (b). Bandwidth estimates are summarised in Table II, $f_{\mathrm{BW},t_{\mathrm{rise}}}$.

TABLE II
BANDWIDTH ESTIMATES BASED ON MEASURED RESPONSES

| Stator | $f_{\mathrm{BW},t_{\mathrm{rise}}}$ | $f_{\mathrm{BW},-3\mathrm{dB}}$ |
|---|---|---|
| Solid, $i_a = 2.5$A ($i_a = 2$A) | 4.9 Hz | (15 Hz) |
| Solid, $i_a = 10$A | 4.6 Hz | – |
| 32 slits, $i_a = 2.5$A ($i_a = 2$A) | 5.2 Hz | (24 Hz) |
| 32 slits, $i_a = 10$A | 4.7 Hz | – |

$f_{\mathrm{BW},-3\mathrm{dB}}$ and $f_{\mathrm{BW},t_{\mathrm{rise}}}$ based on the measured sinusoidal and step force responses.

## D. AMB–Rotor Model Identification

The thrust AMB with the slit stator was assembled as part of the MMW machine [11]. Fig. 18 shows the frequency response to the pseudorandom binary sequence (PRBS) excitation current when levitating the MMW rotor (Fig. 7) with the initial controller. Based on the equations presented in the methods section, the proposed AMB–rotor model was fitted to the frequency

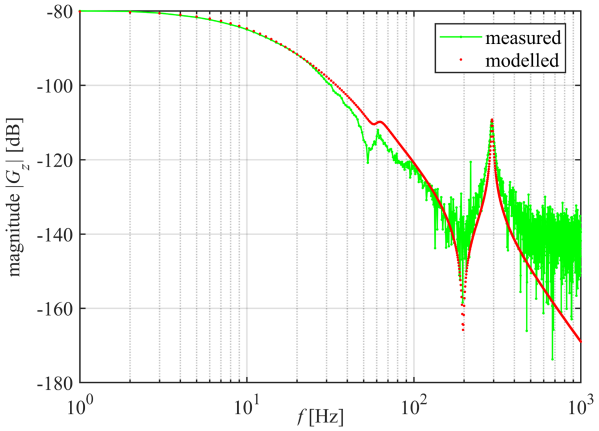


Fig. 18. Magnitude Bode plot of the open-loop (physical plant transfer function in [m/A]) axial AMB plant $G_z$ measured for the drivetrain shown in Fig. 7.

responses. The stiffness coefficients used in the tuned plant model are based on the FEM as given in Table IV, whereas the cornering frequencies and resonant mode coefficients are given in Table V in Appendix. With this control plant model, the model-based optimal controller was synthesized, and achieved an improved closed-loop performance.

Including two mechanical resonances in the plant model effectively allows active damping by the model-based controller. This is limited by the actuator bandwidth, but might still be needed in some applications. For the case study drivetrain, the lower frequency region around 30 Hz was more important for improving the closed-loop performance.

## V. Discussion

In the FEM, we employed static and time-stepping simulations. We found that depending on the bandwidth estimation techniques, the results can vary significantly. The forces obtained by the FEM are sensitive to the number of elements on the pole surfaces and are smaller for less dense meshes. Especially, a sufficiently dense mesh in the main flux paths is required. The forces are very close for rotating and nonrotating shafts because of unipolar fluxes, even with eddy current effects enabled in the 3-D FEM. However, for the nonrotating case, less fluctuations and a better nonlinear convergence are observed because of the static mesh and for numerical reasons. The static FEM force computation provides fast initial results. The force step responses yield an overconservative qualitative performance comparison and are numerically sensitive. The frequency time-stepping derived responses from the FEM are our preferred performance estimation method (Figs. 11 and 12).

The *LR* serial model measurements were performed with two alternative methods, with an *LCR* meter and with a separate constant current supply. The *LCR* meter results, which use variable small current amplitudes (limited by the device power output) at each frequency, lead to an inaccurate bandwidth estimate, as is shown in the FEM and measurement results section. Therefore, only the results from measurements carried out with a separate constant current supply should be compared with the simulation results.

Like in the FEM, also in the measurements, the results at higher amplitudes deviate from the low signal amplitudes, e.g., Fig. 13 versus Fig. 14(a). Higher signal amplitudes provide more practical measurement results. The lower measured inductance values at high frequencies imply a smaller flux linkage (and force) changes for the same current changes. This leads to a higher bandwidth of force responses despite the lower bandwidth of the current responses for the slit stator compared with the solid one [i.e., Fig 14(b)].

Because of the lower frequency limitation of the power supply, when estimating bandwidth based on the measured serial parameters, the inductance values had to be extrapolated at very low frequencies. The bandwidth estimates from the FEM when using sinusoidal current excitation are in line with the equivalent responses measured at 2 A sinusoidal currents. The simulated and measured (with force transducers) step force responses follow the same trends, but the obtained values are further apart.

According to the step force responses from the 3-D FEM, for high-signal amplitudes, the high-amplitude force bandwidth can be increased by 85% and 125% by using 32 and 64 stator slits, respectively. Overall, the estimated bandwidth gains based on the measured force step responses for the 32-slit stator versus the solid one are smaller compared with the FEM (the first method). The bandwidth estimates based on the measured frequency responses (derived from the computed serial model parameters) at 2 A are higher compared with the FEM, the second method emulating frequency responses and evaluating the –3 dB force drop. The analytically estimated bandwidths at small signal amplitudes and at a high bias give the highest values. This relation between the measured and FEM-simulated (using the second method) bandwidths can be explained by the bandwidth being significantly dependent on the current amplitudes as seen in Fig. 11(b). In the case of simulated frequency responses, the bandwidths for the actuators with 32 and 64 slits increased by 75% and 102%, respectively, versus the solid one. In the measured frequency responses at 2 A current amplitudes, the bandwidth for the actuator with 32 slits increased by 60%.

Measuring force responses to the step currents with high current values and small air gaps was challenging because of the mechanical rigidity and difficulty in keeping the same reference air gap when changing stators. In Fig. 17(b), an incorrect reference current step was applied at 8.75 A.

In most systems, higher order dynamics of the actuator (15) and the rotor (16) might not be needed. However, the identification results were obtained from the MMW working as part of a drivetrain comprising flexural coupling and a load machine as in Fig. 7. The complex plant model necessary for fitting the thrust AMB dynamics is attributed to the presence of machine frame modes and multirotor plant. With more patience or using optimization tools, a much better fit of the model to the experimental data can be reached (Fig. 18). The tools for sufficient model formulation are detailed in (14), (15), and (16). Alternatively, one can propose an uncertain weight or uncertain model parameters to facilitate low gain plant variations and added resonances associated with the application. In such cases, $\mu$-synthesis controller can be used, to achieve robust performance while maintaining stability [16], instead of other optimal control methods.

Segmenting or slitting the stator core reduces the effective air gap area and marginally reduces the maximum force capacity of an actuator if the slits are narrow. In this example, 32 slits with a width of 0.5 mm lead also to 5.33 times the high stator core cost. This is feasible only in high-performance applications. On the other hand, increasing the slit width facilitates manufacturing and potentially reduces the cost at the expense of the maximum force capacity.

If segmentation is applied, the mechanical integrity is challenging for tight manufacturing requirements and small air gaps. Compared with segmentation, slitting retains the stator piece integrity and eases the assembly. Still, for great slit depths and thin stator yokes, the mechanical stress should be computed in worst-case conditions to ensure that the maximum deformations are within acceptable limits.

## VI. Conclusion

In the solid thrust AMB, the eddy currents on the pole surfaces affect the electrical parameters, adding to the nonlinear force characteristics because of magnetic saturation. Effective methods to reduce eddy currents and increase the force slue rate and bandwidth are to divide the stator core into smaller segments or to slit the core in the radial direction. The bandwidth of the AMB with solid, slit, and segmented stators was studied using static and time-stepping 3-D FEM simulations. Saturation, leakage, fringing, rotation, voltage limitation, and effects of inner control loop implementation were also considered. The estimates vary greatly depending on excitation amplitudes and whether sinusoidal or step excitation responses are used.

The simulation and measurement results both confirm that the bandwidth of an axial AMB with a solid stator core can be increased by segmenting or slitting. In the case of responses to sinusoidal currents, the bandwidth increases for an increasing number of slits, decreasing current amplitudes, and an increasing depth of slits. The study also presents a novel method to calculate the bandwidth of the actuator with the 3-D FEM with time-stepping simulation by using a dynamic force response method. This requires that the skin depth meshing conditions on the surfaces and eddy current effects are taken into account. According to the simulation results, the segmentation provides an even better performance than the slits. The more comprehensive optimization of the slit structure is left for future studies.

Finally, the overall control plant employing the slit AMB stator was modeled and experimentally identified using PRBS excitation for control purposes in an MMW multirotor application. The model can be assembled with the rotor modes in a parallel connection, and the actuator dynamics, including eddy current effects but linearized in the operating point, in a series connection. The required number of modes and order varies depending on the machine configuration and performance required. Generally, orders are smaller for rigid single rotor applications and higher for multirotor or flexible tubing systems. The increased model accuracy leads to an improved closed-loop control performance and robustness in terms of measured maximum orbit amplitudes and sensitivity peaks.

## Appendix

### TABLE III
Axial AMB – Geometry and Electrical Parameters based on [11]

| Parameter | Value |
|---|---|
| Inner pole inner diameter, $d_1$ [mm] | 102.5 |
| Inner pole outer diameter, $d_2$ [mm] | 129 |
| Outer pole inner diameter, $d_3$ [mm] | 161 |
| Outer pole outer diameter, $d_4$ [mm] | 179 |
| Back iron thickness (disc thickness total) [mm] | 13.5 (13) |
| Outer (inner) disc diameter [mm] | 180 (88) |
| Coil high, $H_{\mathrm{coil}}$ [mm] | 14 |
| Nominal air-gap (clearance) length, $z_0$ [mm] | 0.7 (0.5) |
| Mass of MMW rotor with a coupling flange, $m$ [kg] | 380 |
| Number of turns, $N$ | 71 |
| Material | S355J2 |
| Peak current from the amplifier $i_{\max}$ [A] | 21 |
| Bias current $i_{\mathrm{b}}$ (maximum control current) [A] | 7 (14) |
| DC link voltage $u_{\mathrm{DC}}$ [V] | 565 |

### TABLE IV
Axial AMB – Analytical (And Static FEM) Operational Parameters [11]

| Parameter | Value |
|---|---|
| Nominal inductance (FEM), $L$ [mH] | 16 (26) |
| Resistance, $R$ [$\Omega$] | 0.25 |
| Maximum force (FEM) for one coil active [N] | 6859 (3514) |
| Current stiffness (FEM), $k_i$ [N/A] | 435 (216) |
| Position stiffness (FEM), $k_z$ [N/m] | 4478588 (2177523) |

### TABLE V
Tuned Axial AMB Plant Model Parameters

| Parameter | Value |
|---|---|
| Inner loop filter bandwidth, $\omega_{0\mathrm{p}}$ [rad/s] | $2\pi \cdot 117.4$ |
| Corner frequencies of zeros $\omega_{1\mathrm{z}}$, $\omega_{2\mathrm{z}}$ [rad/s] | $2\pi \cdot 18$, $2\pi \cdot 60$ |
| Corner frequencies of poles $\omega_{1\mathrm{p}}$, $\omega_{2\mathrm{p}}$ [rad/s] | $2\pi \cdot 25$, $2\pi \cdot 40$ |
| Frequency of resonance mode, $\omega_1$, $\omega_2$ [rad/s] | $2\pi \cdot 61$, $2\pi \cdot 294$ |
| Relative damping of resonance mode, $\gamma_1$, $\gamma_2$ | 0.1, 0.01 |
| Mode shape coefficients scaled by $k_i$, $d_1 k_i$, $d_2 k_i$ [N/A] | db2mag(-132)$\omega_1{}^2$, db2mag(-134)$\omega_2{}^2$ |
| Mass fitted to responses of drivetrain $m_0$ [kg] | $1.1 \cdot m$ |

## Acknowledgment

This work was carried on the side of several projects over a few years without dedicated funding. Still, the authors would like to acknowledge: the Academy of Finland (270012, 304071, 350880), and ABB Oy Drives. Atte Putkonen, M.Sc., assisted in capturing AMB–rotor frequency response data and step force responses, and design engineer Kimmo Tolsa, M.Sc., helped with measurements using a Pacific Power Amplifier 360AMX and a Rhode&Schwarz RTO 1014 oscilloscope. Design engineer Toni Kangasmäki helped with dimension drawing in Fig. 2.

## REFERENCES


[1] R. C. Pampreen, *Compressor surge and stall*. Vermont, USA: Concepts ETI; 1st edition, 1993.

[2] S. Yoon, Z. Lin, and P. Allaire, "Experimental evaluation of a surge controller for an AMB supported compressor in the presence of piping acoustics," *IEEE Trans. Control Syst. Technol.*, vol. 22, no. 3, pp. 1215–1223, May 2014.

[3] S. Y. Yoon, Z. Lin, and P. E. Allaire, "On the control of single stage centrifugal compressor surge with active magnetic bearings," in *Proc. 13th Int. Symp. Magn. Bearings*, Arlington, VA, 2012, pp. 1–11.

[4] E. Kurvinen, R. Fittro, and E. Maslen, "Improving compressor surge performance with advanced control," in *Proc. Inst. Mech. Engineers. Part I: J. Syst. Control Eng.*, vol. 230, no. 7, 2016, pp. 672–679, .

[5] J. Passenbrunner, G. Jungmayr, and W. Amrhein, "Simulation and optimization of the starting behavior of an active axial bearing with viscoelastic damping support," in *Proc. IEEE Int. Electric Machines Drives Conf.*, 2017, pp. 1–6.

[6] H. Walter, J. Denk, and B.-U. Koehler, "Specification and Judging of High-Speed Rotating Machinery With AMB–A Practical Guideline for OEMs, EPC, and End Users," *IEEE Trans. Ind. Appl.*, vol. 50, no. 2, pp. 1521–1529, Mar./Apr. 2014.

[7] L. Zhou and L. Li, "Modeling and identification of a solid-core active magnetic bearing including eddy currents," *IEEE/ASME Trans. Mechatronics*, vol. 21, no. 6, pp. 2784–2792, Dec. 2016.

[8] Z. W. Whitlow, R. L. Fittro, and C. R. Knospe, "Dynamic performance of segmented active magnetic thrust bearings," *IEEE Trans. Magn.*, vol. 52, no. 11, pp. 1–11, Nov. 2016.

[9] H. Spece, R. Fittro, and C. Knospe, "Optimization of axial magnetic bearing actuators for dynamic performance," *Actuators*, vol. 7, no. 66, pp. 1–15, 2018.

[10] S.-H. Park and C.-W. Lee, "Decoupled control of a disk-type rotor equipped with a three-pole hybrid magnetic bearing," *IEEE/ASME Trans. Mechatronics*, vol. 15, no. 5, pp. 793–804, Oct. 2010.

[11] R. P. Jastrzebski, A. Putkonen, E. Kurvinen, and O. Pyrhonen, "Design and modeling of 2 MW AMB rotor with three radial bearing-sensor planes," *IEEE Trans. Ind. Appl.*, vol. 57, no. 6, pp. 6892–6902, Nov./Dec. 2021.

[12] R. P. Jastrzebski, E. Kurvinen, and O. Pyrhönen, "Design, modelling and control of MIMO AMB system with 3 radial bearing planes for megawatt-range high-speed rotor," in *Proc. IEEE Int. Electric Machines Drives Conf.*, 2019, pp. 805–811.

[13] P. Jaatinen, T. Sillanpaa, R. P. Jastrzebski, E. Sikanen, and O. Pyrhonen, "Automated parameter identification platform for magnetic levitation systems: Case bearingless machine," in *Proc. 15th Int. Symp. Magn. Bearings*, 2016, pp. 275–281.

[14] R. P. Jastrzebski, P. Jaatinen, O. Pyrhonen, and A. Chiba, "Design optimization of permanent magnet bearingless motor using differential evolution," in *Proc. IEEE Energy Convers. Congr. Expo.*, 2018, pp. 2327–2334.

[15] R. P. Jastrzebski, P. Jaatinen, T. Sillanpaa, E. Sikanen, and O. Pyrhonen, "Automated design of AMB rotor systems with standard drive, control software and hardware technologies," in *Proc. 15th Int. Symp. Magn. Bearings*, 2016, pp. 78–85.

[16] F. Aghili, "Robust impedance-matching of manipulators interacting with uncertain environments: Application to task verification of the space station's dexterous manipulator," *IEEE/ASME Trans. Mechatronics*, vol. 24, no. 4, pp. 1565–1576, Aug. 2019.


**Rafal Piotr Jastrzebski** (Senior Member, IEEE) received the M.Sc. degree in microelectronics from the Technical University of Lodz, Lodz, Poland, in 2002, and the D.Sc. degree in electrical engineering from the Lappeenranta-Lahti University of Technology (LUT), Lappeenranta, Finland, in 2007.

He worked as researcher in Poland, Germany, Japan, and Finland. He is currently an Associate Professor (tenured) with the University of Turku, Turku, Finland, and Docent with LUT in modelling and control of electromechanical systems. His research interests include mechatronic systems, digital control, energy applications, active magnetic bearings, magnetic levitation systems, and bearingless machines.

Dr. Jastrzebski was an Academy of Finland Postdoctoral Researcher from 2009 to 2011 and an Academy Research Fellow from 2013 to 2018.

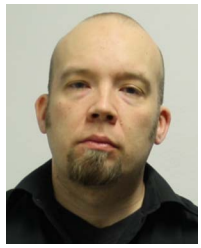

**Olli Liukkonen** received the M.Sc. degree in electrical engineering from Helsinki University of Technology, Espoo, Finland, in 2005. He is currently working toward the Ph.D. degree in electrical engineering with the Lappeenranta–Lahti University of Technology (LUT), Lappeenranta, Finland.

He is also working as Senior R&D Engineer with ABB Oy Large Motors and Generators, Technology Development, Helsinki, Finland. In his 19 years with electrical machines he has been primarily working in areas of testing, electromagnetic design, and development of high speed machines. His research interests include design, modeling, and control of electric machines, FEM, and friction losses.